Model Metal-Oxide Electrocatalysts for Energy Conversion

Modelové elektrokatalyzátory kov-oxid pro konverze energie

Modellsysteme für Metall-Oxid-Elektrokatalysatoren im Bereich der Energieumwandlung

under Cotutelle agreement between

Matematicko-fyzikální fakulta Univerzity Karlovy, Praha

Der Naturwissenschaftlichen Fakultät der Friedrich-Alexander-Universität Erlangen-Nürnberg

for obtaining a doctoral title Ph.D./Dr. rer. Nat.
submitted by

Lukáš Fusek

from Prague

Abstract

The development of novel (electro-)catalysts is commonly based on a trial-and-error approach without detailed understanding of the catalytic processes at the atomic scale. Reaching such understanding would be desirable, but, practically, it is not possible with real catalysts due to their structural and chemical complexity, and the presence of reaction environment. These limitations can be overcome following the model catalysis approach. In this thesis the elementary aspects of model catalysis are applied on electrochemical reactions to reach detailed understanding of fundamental electrocatalytic processes at the atomic level of various catalysts applicable in energetically relevant reactions. The studied model catalysts consist of rare metals (Pd, Pt) and reducible oxides (Co_3O_4, CeO_2). The main focus lied on the study of morphological and chemical properties of these systems in ultrahigh vacuum (UHV) and electrochemical environment combining surface science and electrochemical methods. The results show a clear link between the structural properties of the catalysts and their stability and performance in the electrochemical environment. The obtained level of understanding allows us to define key parameters to optimize the catalyst properties, identify adsorption sites and describe the elementary steps of catalytic reactions.

Results

This thesis focuses on model studies of metal and metal-oxide catalysts applicable in energetically relevant electrochemical reactions. The presented studies address all four aspects of model catalysis – morphology and chemical state of the catalyst, stability of the catalyst, adsorption properties, and reaction pathways – described in Section 1.2. and demonstrate that by using a proper combination of experimental techniques it is possible to answer all of them. The studied catalytical systems vary from metal single-crystal through continuous oxide film to metal-oxide catalyst in both – classical and inverse – geometry covering a wide range of chemical and morphological complexity. Each system addresses specific questions about a particular catalyst.

Firstly, a model study of atomically dispersed Pt catalyst on a $Co_3O_4(111)$ is presented. The study focus on the chemical state of the supported Pt nanoparticles, and their properties and stability under various UHV conditions. Sections 4.2. – 4.4. present a detailed study on the stability and properties of the active metal phase of $Pd/Co_3O_4(111)$ catalyst. Namely, Section 4.2 represent an analogous study to Section 4.1 describing the growth of Pd nanoparticles on $Co_3O_4(111)$ substrate from the initial state of nucleation, the formation of $Pd/Co_3O_4(111)$ interface and the EMSI. In the next step, a thermodynamical stability of these nanoparticles when exposed to oxidizing or humid conditions using near ambient pressure XPS is investigated (Section 4.3.). Finally, Section 4.4 deal with the stability of Pd nanoparticles supported on $Co_3O_4(111)$ and highly oriented pyrolitic graphite (HOPG) in alkaline electrolytes (Section 4.4.).

All so far mentioned studies investigate the metal-oxide catalyst in conventional geometry. Therefore, the main focus lies on the properties and stability of the metal phase. Section 4.5 represents a model study of inverse metal-oxide catalyst, which focuses on the properties and stability of the oxide phase. Namely, it is the stability of CeO_2/Pt catalyst in alkaline electrolyte as a function of applied potential, the size of ceria nanoislands, and the preparation method.

In sections 4.1-4.5 we addressed the first two aspects of model catalysis – morphology and properties of the catalyst and its stability under electrochemical conditions. In Section 4.6, we move on to the third aspect – adsorption properties. Monophosphonatophenyltriphenyl

porphyrin (MPTPP) was anchored to atomically defined Co3O4(111) film and its binding motif was identified by EC-IRRAS.

Finally, Section 4.7. addresses the last aspect – the electrocatalytical reaction itself. The dehydrogenation of 1-cyclohexyl ethanol, which may serve as a potential electrochemically active LOHC, is studied using Pt single-crystal catalysts. The electrooxidation products were identified by EC-IRRAS.

[P1] – Atomistic picture of metal support interaction and role of water

The STM image of the as-prepared $Co_3O_4(111)$ film reveals well-ordered terraces terminated by Co^{2+} cations with two types of structural features – bright protrusions (marked with yellow circle, hereafter denoted as species I) and dark depressions (marked with blue circle, hereafter denoted as species II). The species I disappear after deposition of Pt, but two additional types of species appear – bright protrusions in registry with $Co_3O_4(111)$ (marked with green circle, hereafter denoted as species III) and triangular shaped large bright protrusions in threefold hollow sites (marked with red circle, hereafter denoted as species IV). Apart from that, larger bright species X were identified at Pt coverages of 0.04 and 0.10 MLE (marked with orange circle), which are assigned to small $Pt^{\delta+}$ aggregates.

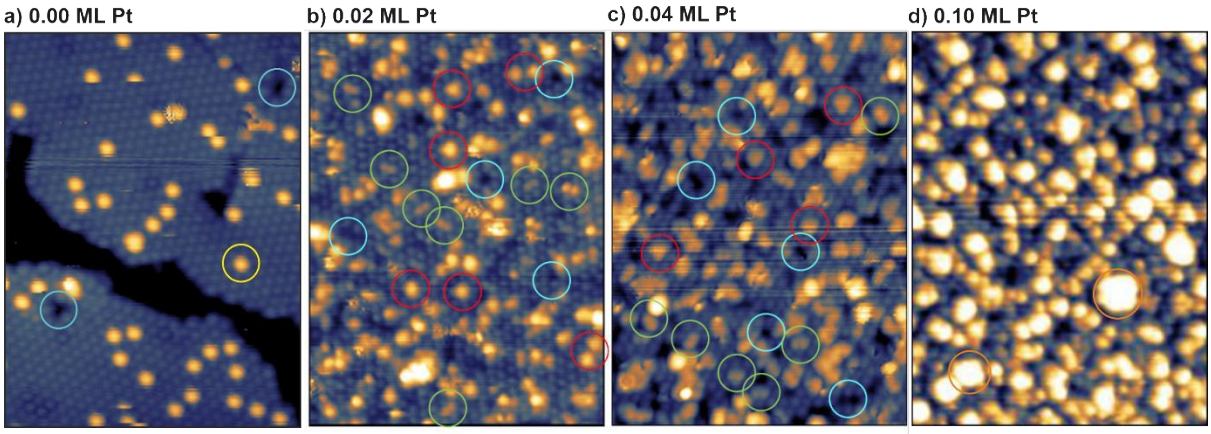

Figure P1.1: STM images a) Co3O4(111) b) 0.02 ML Pt/Co3O4(111) c) 0.04 ML Pt/Co3O4(111) d) 0.13 ML Pt/Co3O4(111)

In order to identify the nature of species I-IV, theoretical group of prof. S. Piccinin[1] simulated STM images of various surface configurations with density functional theory (DFT) using the Tersoff-Hamann approximation. Species I represent a single OH^- group on top of Co^{2+} cation with H^+ on a neighboring oxygen anion. For Species II, DFT calculations suggest that the dark depressions are voids caused by missing surface Co^{2+} cation. The most probable interpretation of species III appearing after Pt deposition is Pt atoms substituting Co^{2+} cations. This interpretation represents also the most energetically favorable configuration of adsorbing Pt single atoms. Finally, species IV are attributed to so called triaqua complexes – Pt atoms in FCC sites decorated by three OH^- groups interacting with three H^+ cations adsorbed on the surrounding oxygen cations.

[1] DFT calculations were performed by theoretical group of prof. S. Piccinin from Istituto Officina dei Materiali, Consiglio Nazionale delle Richerche, Trieste

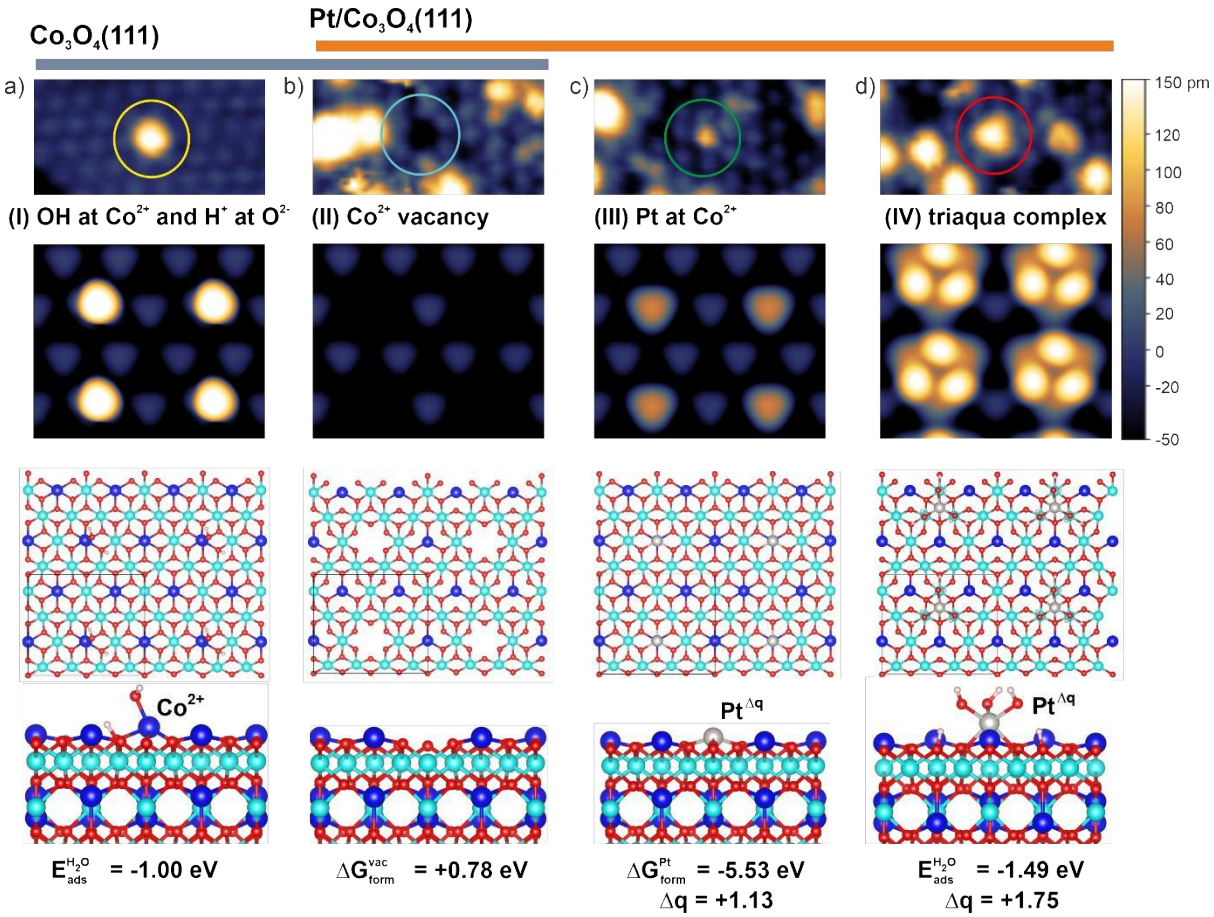

Figure P1.2: Interpretation of species I-IV based on DFT calculations.

There are two doublets in the Pt 4f region. The first doublet at 72.3 eV, can be assigned either to atomically dispersed Pt^{2+} cations or to ultra-small $Pt^{\delta+}$ aggregates. The second doublet at 74.0 eV represents Pt^{4+} species.

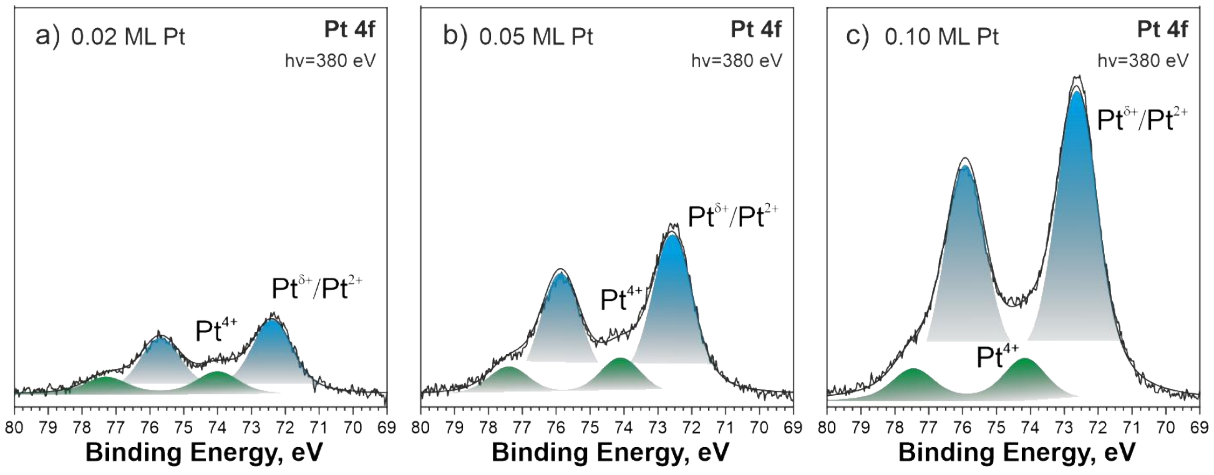

Figure P1.3: SRPES Pd 4f spectra a) 0.02 ML Pt b) 0.04 ML Pt c) 0.10 ML Pt.

To further investigate the role of water on the atomic dispersion of Pt, 0.1 MLE of Pt was deposited on three types of $Co_3O_4(111)$ – dehydroxylated, hydroxylated and moist. The as-prepared samples predominantly consist of Pt^{2+} substituting Co^{2+} cations, Pt^{4+} triaqua complexes and ultra-small $Pt^{\delta+}$ aggregates. The amount of Pt^{4+} upon deposition is similar for all three samples. Annealing to 350 K lead to formation of triaqua complexes accompanied by increase of Pt^{4+} and decrease of Pt^{2+}/ $Pt^{\delta+}$ signal. This tendency is more pronounced on the

moist sample. Water stabilizes Pt at FCC sites or relocate Pt^{2+}/ $Pt^{\delta+}$ to the FCC position forming triaqua complexes. However, after the loss of the hydroxyl group, Pt at the FCC sites are prone to sintering. Therefore, with further annealing, Pt^{4+} species are reduced to Pt^{2+}/ $Pt^{\delta+}$ and further to metallic Pt^0 above 450 K with the highest amount of Pt^0 for the moist sample.

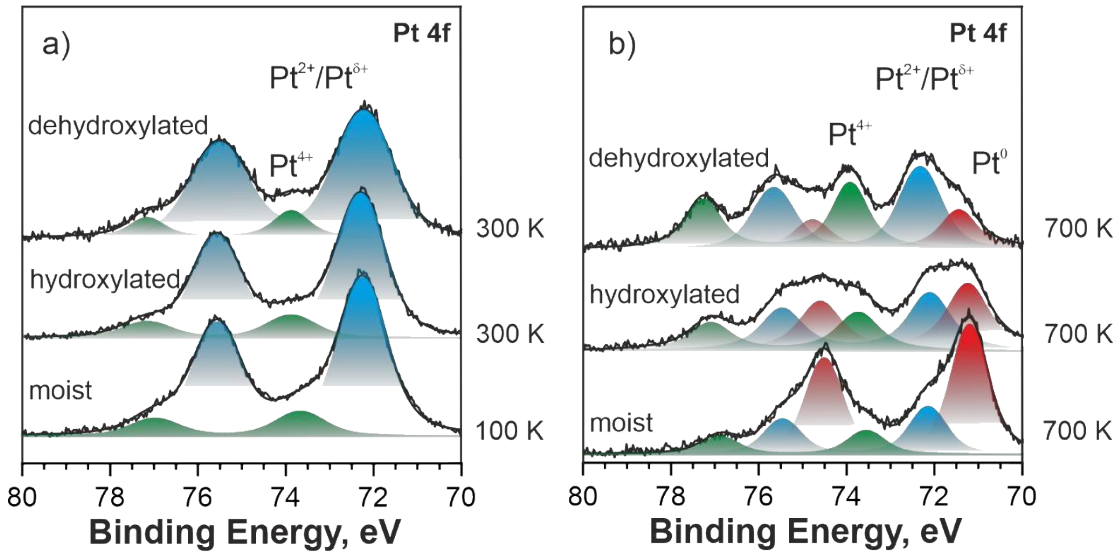

Figure P1.4: Pt 4f spectrum of dehydroxylated, hydroxylated and moist sample a) as prepared b) after annealing at 700 K.

[P2] – Pd/Co_3O_4(111) interface formation

STM images of Pd nanoparticles with the coverages of 0.06 MLE, 0.18 MLE, and 1.91 MLE show that Pd nanoparticles are homogeneously dispersed on the Co_3O_4(111) surface. At low coverages, Pd forms small clusters with a characteristic size of approximately 1 nm. These clusters coalesce at higher coverage and form flat faceted islands of several nanometers.

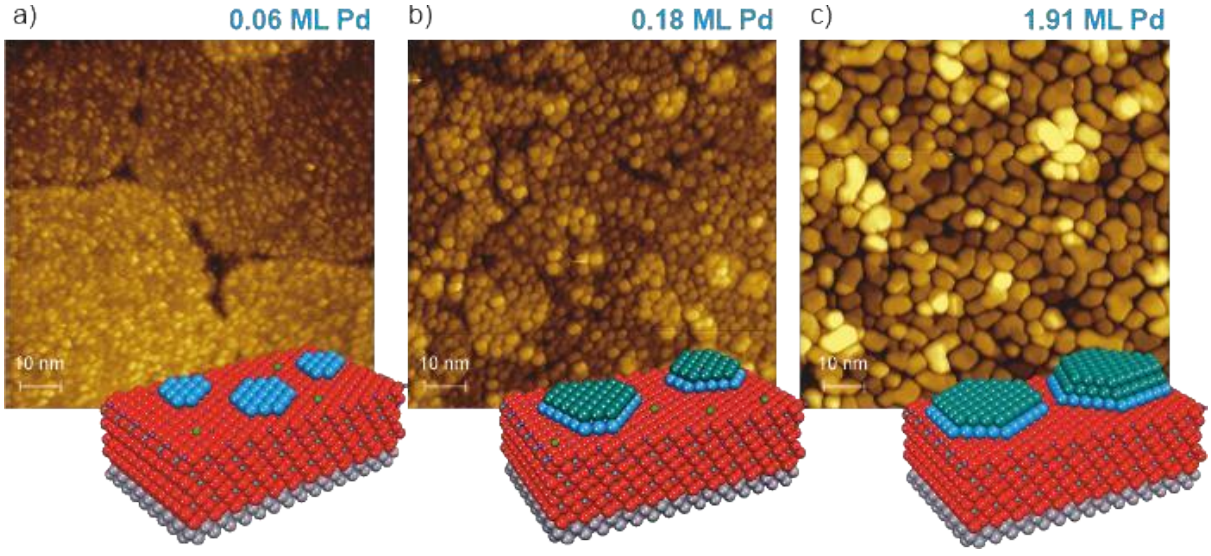

Figure P2.1: STM images of Co_3O_4 supported Pd nanoparticles. a) 0.06 ML b) 0.18 ML c) 1.91 ML.

For small coverages of 0.05 MLE and 0.19 MLE, SRPES measurements show two doublets in the Pd 3d spectrum at 337.1 eV and 338.4 eV. Peaks might be assigned to small $Pd^{\delta+}$ metallic aggregates or PdO_x clusters, and atomically dispersed Pd^{2+} ions, respectively. With increasing coverage, an additional doublet appears at 336.2 eV and shifts towards lower binding energy

reaching 335.7 eV. This behavior corresponds well with the growth of larger Pd^0 nanoparticles with Pd^{2+} and $Pd^{\delta+}$ serving as a nuclei for Pd^0 nanoparticles. The depth profiling shows that metallic Pd^0 covers Pd^{2+} and $Pd^{\delta+}$, which form the $Pd/Co_3O_4(111)$ interface.

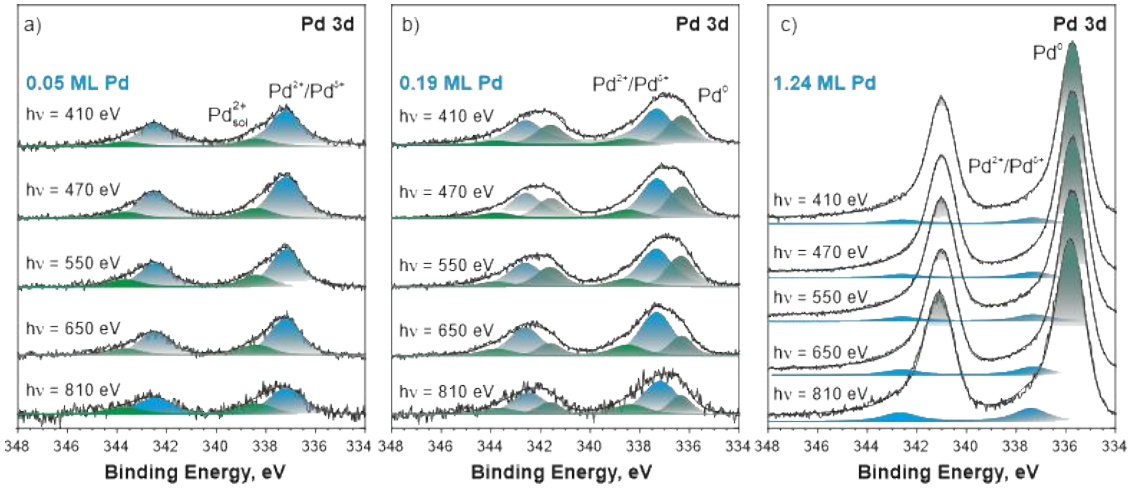

Figure P2.2: SRPES, Pd 3d spectra a) 0.05 ML b) 0.19 ML c) 1.24 ML.

Finally, the charge transfer at the $Pd/Co_3O_4(111)$ interface was analyzed by comparing Co^{2+} and Co^{3+} intensities in the valence band spectra obtained with photon energy of 60 eV and in the resonant photoemission spectra. The charge transfer is affecting the first two Co layers. Firstly, there is a preferential reduction of a small fraction of Co^{3+} in the first layer, which is most probably located at defect sites. Afterwards, the second layer consisting of Co^{3+} ions is reduced until the ratio reaches 1 at the coverage of 1.24 MLE.

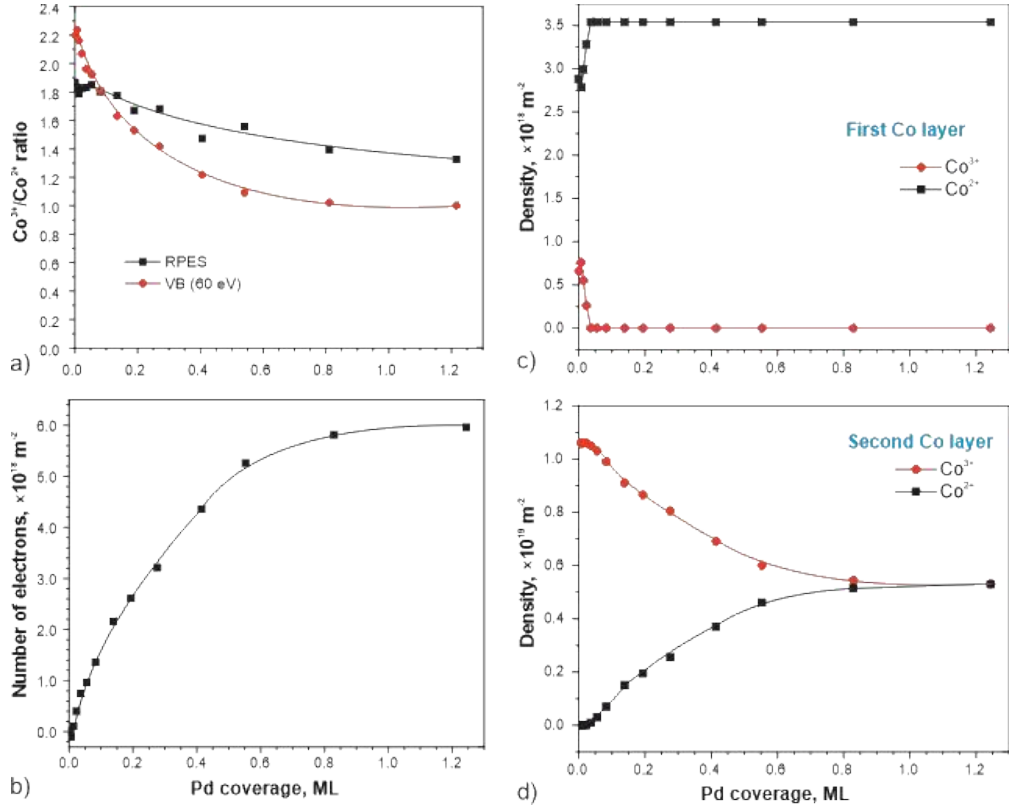

Figure P2.3: Pd coverage dependance of a) Co2+/Co3+ ratio b) charge transfer c), d) Co2+ and Co3+ distribution.

[P3] Stability of the Pd/Co_3O_4(111) model catalysts in oxidizing and humid environments

STM showed that Pd forms flat nanoislands homogeneously dispersed on the Co_3O_4(111) surface with a characteristic size of 4 nm. The nanoparticles predominantly consist of metallic Pd^0 with a small fraction of Pd^{2+} either in the form of PdO or dissolved in Co_3O_4(111) layer. After annealing at 700 K, Pd nanoparticles sinter and form larger well-faceted cluster with approximately half the density compared to RT. The Pd 3d XPS spectrum remains virtually unchanged.

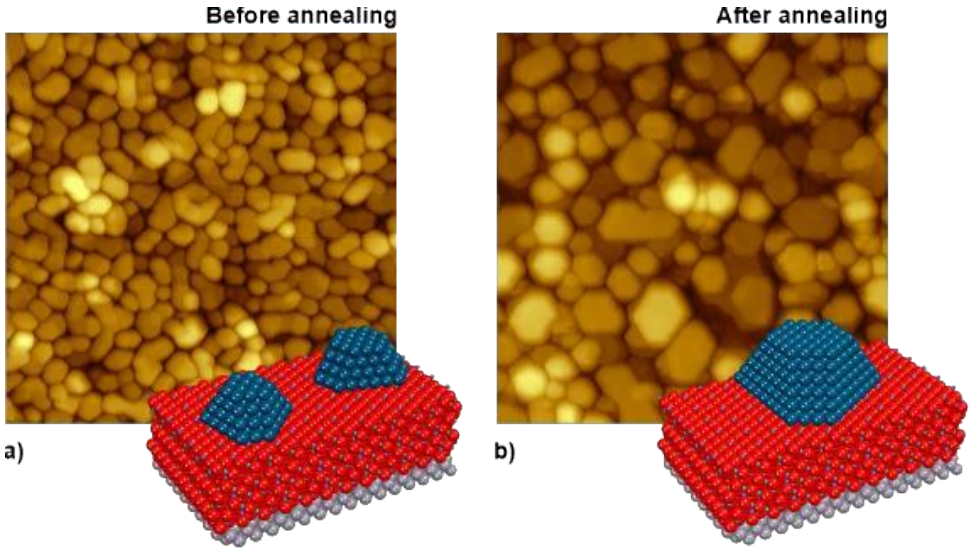

Figure P3.1: STM images of Co_3O_4 supported Pd nanoparticles a) as-prepared b) after annealing to 700 K.

The stability of Pd/Co_3O_4(111) was studied in the NAP cell using a monochromatized Al K-α source. XPS spectra were measured under three different conditions – (i) UHV ($<10^{-8}$ mbar), (ii) 1 mbar O_2, and (iii) evacuated ($<10^{-5}$ mbar) – at constant temperature between 300 K and 700 K. After exposure to 1 mbar of oxygen, contribution 2 associated with formation of PdO increased starting at 300 K. PdO is stable in the whole temperature region 300 – 700 K. PdO decomposes after evacuation of the NAP cell.

After annealing in UHV, Co_3O_4 started to reduce above 500 K with a complete reduction to CoO at 550 K. The CoO is oxidized back to Co_3O_4 after exposure to oxygen and remains oxidized until the next annealing in UHV. The increase of Co^{2+} signal during the redution is coupled with an increase of the Pd contibution 1b at the expanse of contribution 1a. This indicates that oxygen released during Co_3O_4 reduction is dissolved in Pd nanoparticles.

Similar to oxidizing conditions, the stability of Pd nanoparticles under humid conditions was studied. The same experimental procedure was followed where only the step (ii) was replaced by exposure to 1 mbar of H_2O. No changes were observed at temperatures below 450 K. At 450 K, the contribution 1b dramatically increases at the expense of contribution 1a. Similar to oxidizing conditions, this process is coupled with reduction of Co_3O_4 to CoO. In contrast with oxidizing conditions, CoO remains reduced and only minor changes are observed in the spectra above 450 K.

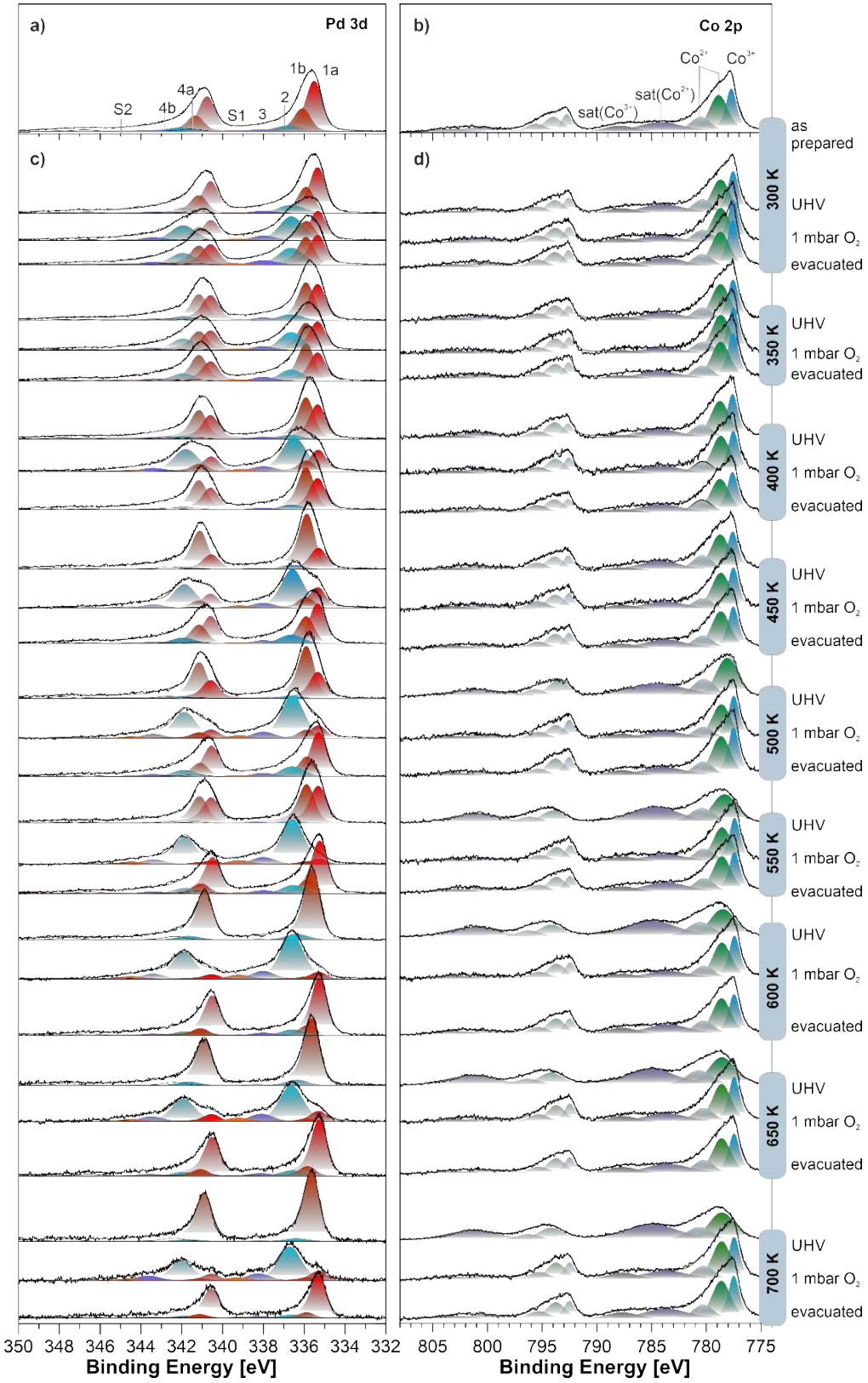

Figure P3.2: NAP-XPS, Pd 3d spectrum (a) and Co 2p spectrum (b) of the as-prepared Pd nanoparticles supported on the $Co_3O_4(111)$. The evolution of XPS spectra during the annealing and exposure to oxygen a) Pd 3d spectra b) Co 2p spectra.

The NAP-XPS data were used to analyze the sintering and dissolution of Pd nanoparticles. During the annealing in UHV, the total intensity of Pd 3d spectra remain unchanged up to 550 K. Above this temperature, a slight decrease was observed caused by sintering of Pd nanoparticles. On the other hand, an intensity dropped significantly during annealing under oxidizing and humid environment.

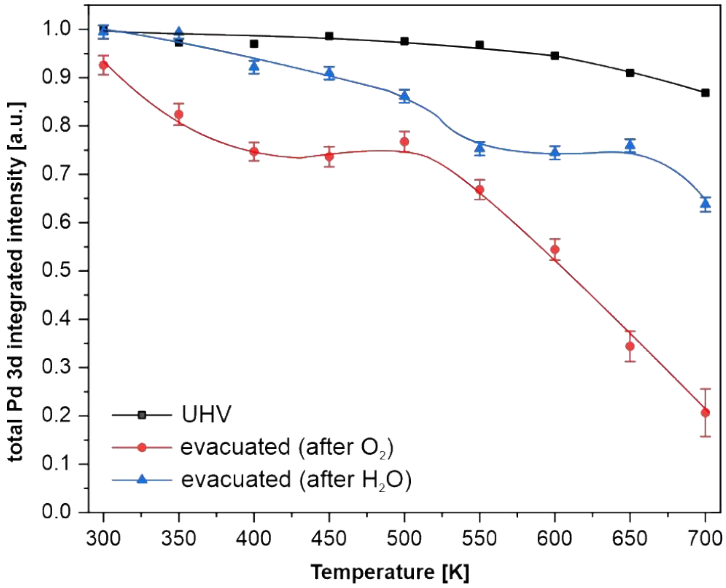

Figure P3.3: Dissolution of Pd. Total Pd 3d intesities after annealing in UHV (black) and during evacuation of the NAP cell after annealing in oxygen (red) and water (blue).

[P4] Particle size and shape effects in electrochemical environments: Pd particles supported on ordered $Co_3O_4(111)$ and highly ordered pyrolytic graphite

The morphology and chemical state of as-prepared Pd nanoparticles on $Co_3O_4(111)$ were discussed in detail in the previous chapters. Pd nanoparticles supported on HOPG show qualitative differences in comparison with those supported on $Co_3O_4(111)$ – Pd nanoparticles are hemispherical with comparable density. Pd nanoparticles on HOPG are predominantly metallic.

An emersion SRPES measurements were performed with photon energies between 410 eV and 930 eV. The whole procedure was repeated for each potential step in the range of 0.5 – 1.5 V_{RHE}. The oxidation state of Pd/HOPG and 2.5 ML Pd/ $Co_3O_4(111)$ is practically unaffected between 0.5 V_{RHE} and 1.1 V_{RHE}. There is only a minor contribution emerging at 338.4 eV for Pd/HOPG at 0.9 V_{RHE} and 1.1 V_{RHE}. This contribution is associated with formation of surface oxide. For both, the formation of PdO starts at 1.3 V_{RHE} and continues at 1.5 V_{RHE}. After emersion at 0.5 V_{RHE} PdO is predominantly reduced back to metallic Pd^0. For 0.15 ML Pd/ $Co_3O_4(111)$, the contribution associated to atomically dispersed Pd^{2+} in $Co_3O_4(111)$ disappears after first emersion at 0.5 V_{RHE}. Afterwards, no changes are observed in the Pd oxidation state.

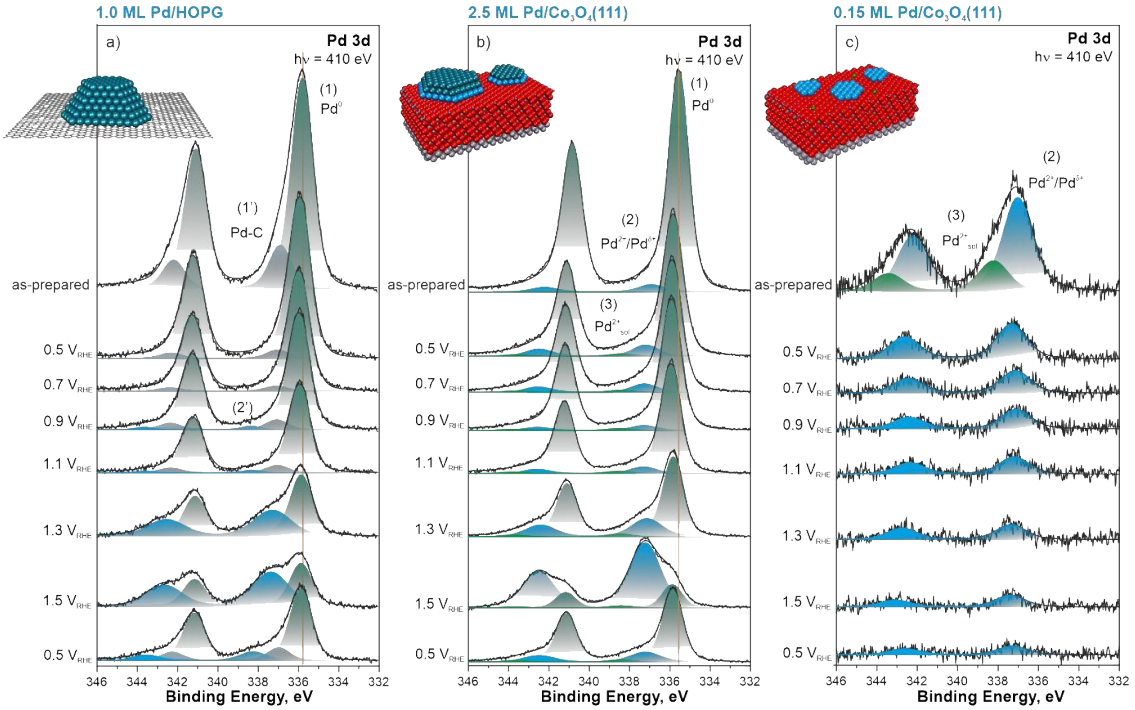

Figure P4.1: SRPES, Pd 3d spectra after after immersion in electrolyte a) 1.0 ML Pd/HOPG b) 2.5 ML Pd/Co_3O_4 c) 0.15 ML Pd/Co_3O_4.

The depth profiles of Pd/HOPG and 2.5 ML Pd/ Co_3O_4(111) after emersion at 1.3 V_{RHE} and 1.5 V_{RHE} show that in both cases PdO is formed on the surface of the nanoparticles. The intensity analysis revealed that the formed PdO covers less than the top layer of the nanoparticles in both cases after emersion at 1.3 V_{RHE}. The coverage remains below a full monolayer for Pd/HOPG after emersion at 1.5 V_{RHE}, but greatly exceeds this amount for Pd/ Co_3O_4(111). Particles with heights of 2 – 3 ML are fully oxidized, whereas, for higher nanoparticles, only the top layer is oxidized.

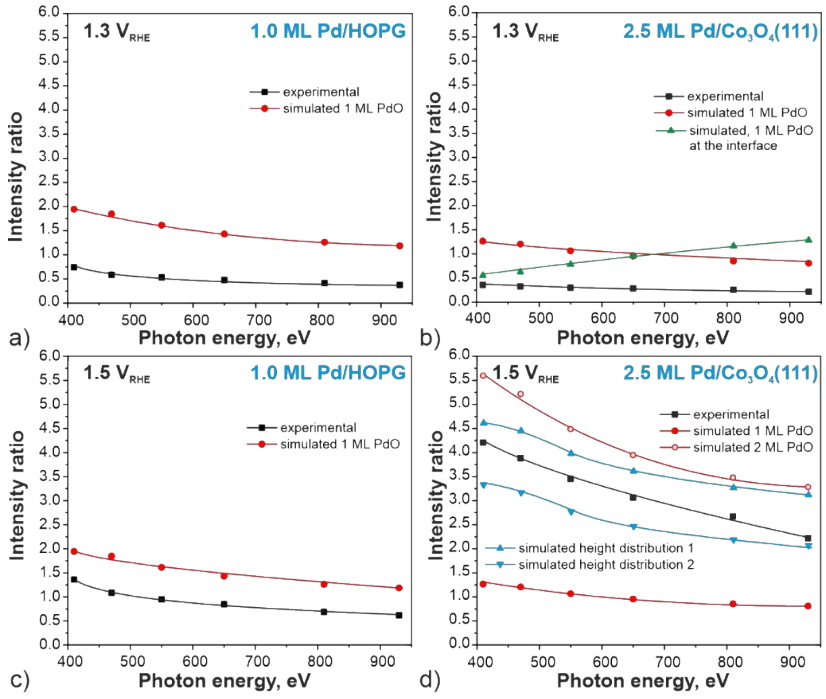

Figure P4. 2: Intensity ratio between metallic Pd and PdO contributions after emersion at a given potencial as a function of photon energy. a) c) Pd/HOPG b) d) Pd/Co_3O_4.

[P5] - Stability, redox properties, and hydrogen intercalation in ceria-Pt model electrocatalyst

Two series of CeO_2(111) nanoislands were deposited onto Pt(111) with varying ceria coverage by two preparation procedures and analyzed with the methods of surface science. STM analysis reveals significant morphological differences between the two series. Ceria nanoislands annealed in the last step to 1050 K, hereafter denoted as high-temperature (HT) samples, show large flat islands with characteristic sizes of tens of nanometers and the island edges aligned with substrate main crystallographic directions. On the other hand, samples annealed in the last step to 850 K, hereafter denoted as low-temperature (LT) samples, results in small but still flat ceria nanoislands with round edges.

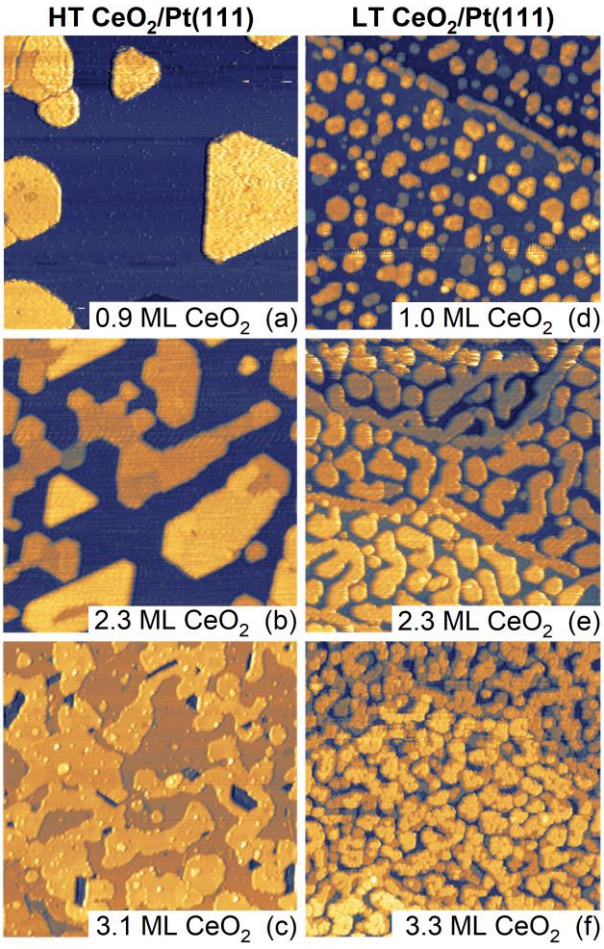

Figure P5.1: STM images (150 × 150 nm^2) of as-prepared CeO_2/Pt(111) model catalysts. a) HT sample, 0.9 MLE, b) HT sample, 2.3 MLE, c) HT sample, 3.1 MLE, d) LT sample 1.0 MLE, e) LT sample 2.3 MLE, f) LT sample, 3.3 MLE.

CVs obtained in 0.1 M KOH between -0.05 V_{RHE} and 0.9 V_{RHE} show electrochemical instability of LT samples. Voltammogram of HT samples doesn't change while cycling. In the case of LT samples, oxidation/reduction pair of peaks at 0 – 0.3 V_{RHE} dimishes and new pair of peaks appears at 0.4 – 0.7 V_{RHE}.

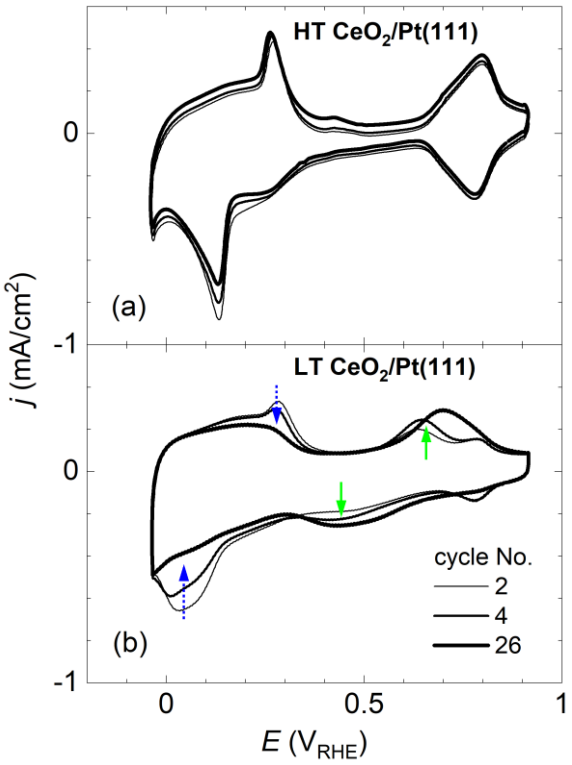

Figure P5.2: Electrochemical stability of HT (top) and LT (bottom) sample – CV cycle dependance.

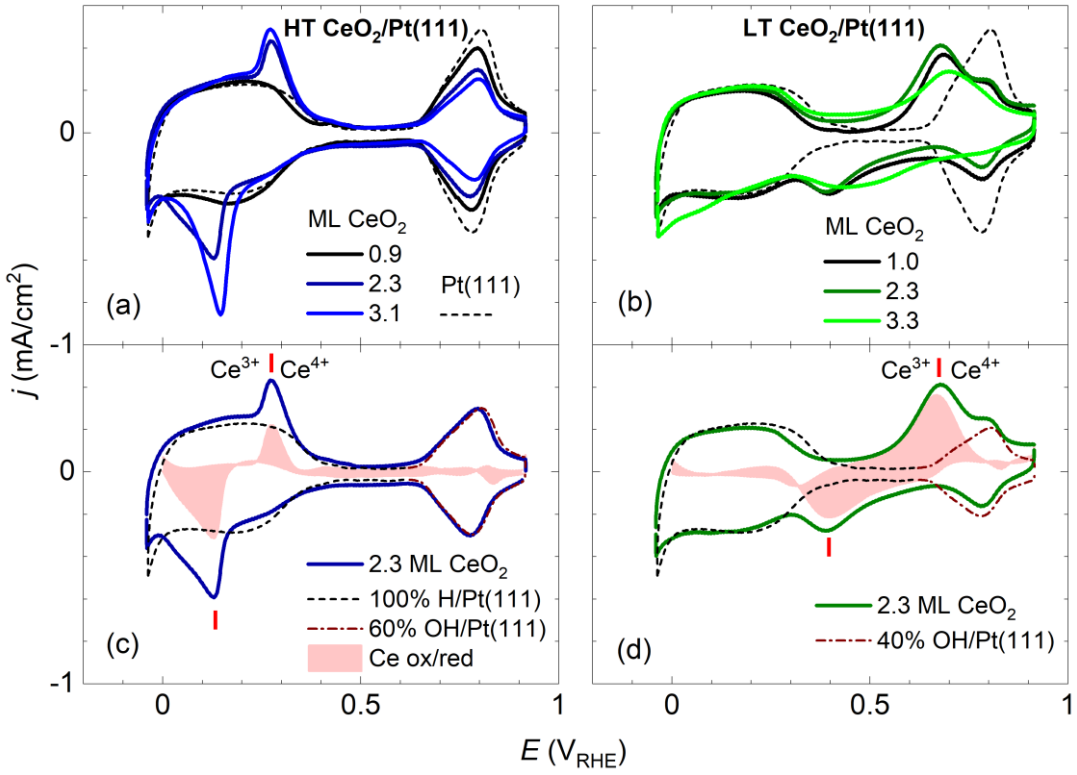

Figure P5.3: Stabilized CVs of HT and LT samples and charge analysis, reference CV of bare Pt(111) (dotted line). a) HT sample, 2.25 ML b) LT sample, 2.25 ML c) charge decomposition of stabilized HT CV, red area – contribution of Ce^{3+}/Ce^{4+} transition d) charge decomposition of stabilized LT CV, red area – contribution of Ce^{3+}/Ce^{4+} transition.

CV of bare Pt(111) serving as a reference (dotted line) shows typical butterfly shape consisting of three distinct regions – H adsorption/desorption at potentials between -0.05 V_{RHE} and 0.35 V_{RHE}, double layer region from 0.35 V_{RHE} to 0.65 V_{RHE}, and OH adsorption/desorption at 0.65 – 0.9 V_{RHE}. In stabilized CVs of ceria, an additional irreversible pair of peaks appears in H adsorption/desorption region for HT samples and, in the LT samples a shifted one in the double layer region. In both cases, the irreversible pair is assigned to Ce^{3+}/Ce^{4+} redox transition.

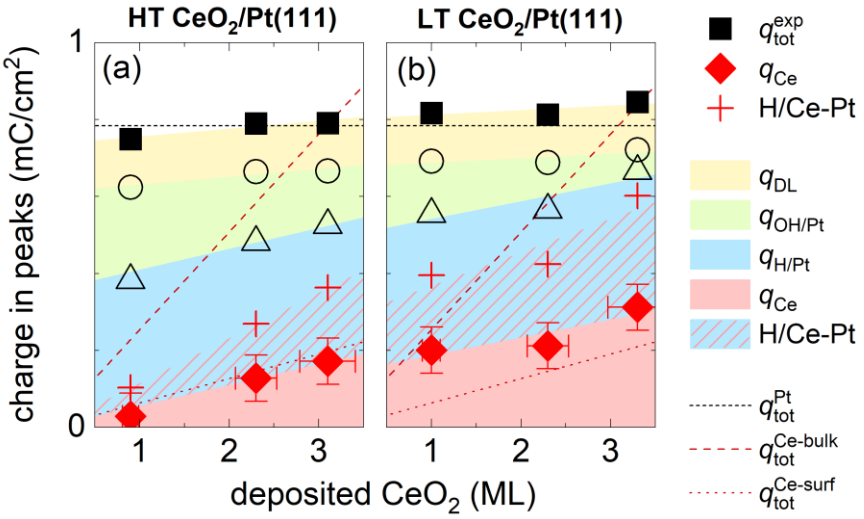

Figure P5.4: Charge contribution in the CVs.

Three main contributions to the total charge correspond to the following processes: the Ce^{3+}/Ce^{4+} transition (q_{Ce}), the H adsorption/desorption on Pt(111) ($q_{H/Pt}$), and the OH adsorption/desorption on Pt(111) ($q_{OH/Pt}$). Additionally, there is a small constant contribution of double layer (q_{DL}), which was determined from reference CV of bare Pt(111).

[P6] Anchoring of porhyrins on atomically defined cobalt oxide: In-situ infrared spectroscopy at the electrified solid/liquid interface

EC-IRRAS spectra were measured in the potential range of 0.3 V_{RHE} – 1.3 V_{RHE} with a step size of 0.1 V. In the anodic scan recorded with p-polarized light, a formation band appears at 1450 cm^{-1} and consumption band appears at 1115 cm^{-1} starting at 0.7 V_{RHE}. Additionally, s-shape band at 970 cm^{-1} appears at 0.9 V_{RHE}. The first two bands are related bending modes of NH_4^+ and NH_3, respectively, which indicates protonation of the ammonia buffer.

The band at 970 cm^{-1} is in the frequency region of phosphonates. We assign this band to the stretching vibration of PO_3^{2-}. Because no other bands related to the porphyrin are observed, we assume that MPTPP binds to the surface via phosphonate group in the form of chelating tridentate – i. e. all three oxygen atoms bind to one surface Co^{2+} ion.

In the cathodic scan, the intensities of all bands decrease with decreasing potential. The porphyrin band at 970 cm^{-1} fully disappears at 0.9 V_{RHE}, which is the same potential at which it appeared. Similarly, the ammonia buffer bands disappear at 0.7 V_{RHE}. This shows that all processes are fully reversible. All bands were observed only with p-polarized light. There are no potential dependent changes in spectra measured with s-polarized light. Therefore, all processes are related to surface species.

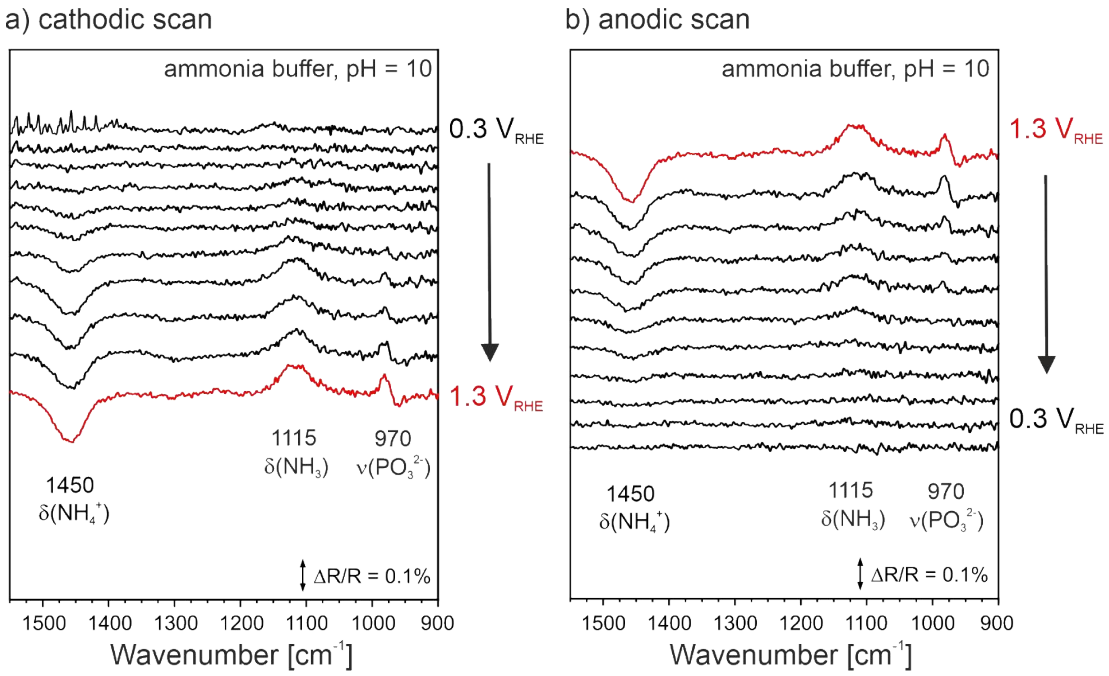

Figure P6.1: EC-IRRAS, $Co_3O_4(111)$ functionalized with MPTPP measured with p-polarized light at the potential window between 0.3 – 1.3 V_{RHE} a) cathodic scan b) anodic scan. Reference spectra measured at 0.3 V_{RHE}.

[P7] Direct fuel cell liquid organic hydrogen carriers: The electrooxidation of cyclohexylethanol

In this work, different possible reaction paths of 1-cyclohexylethanol oxidation are considered with different products.

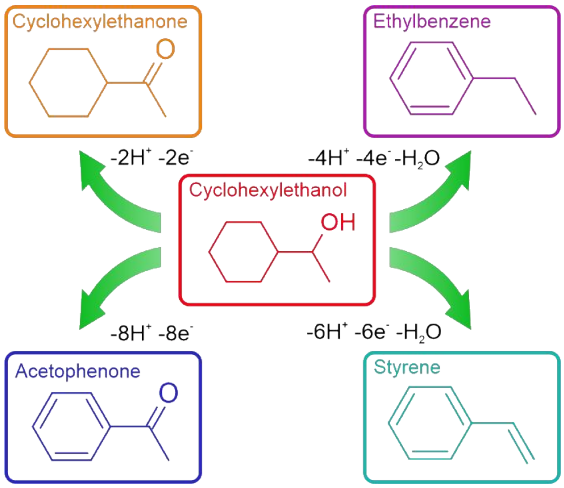

Figure P7.1: Schematic visualization of possible reaction products.

CVs (studied by prof. Thiele's group[2]) of Pt(100), Pt(110) and Pt(111) showed that the highest activity is reached with Pt(111) and the maximum is reached at 0.37 V_{RHE}. The activity of the other two surfaces is approximately one order of magnitude lower. However, the activity quickly drops and the oxidation peak shifts to higher potential during cycling.

[2] CV measurement were performed by group of prof. Simon Thiele, Helmholtz Institute Erlangen-Nürnberg

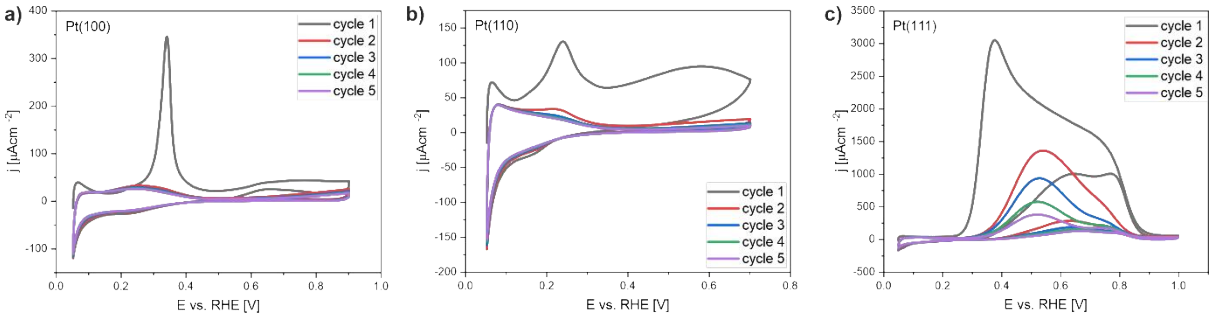

Figure P7.2: CVs of low-index Pt single crystals in 0.1M $HClO_4$ + 0.02 M 1-cyclohexyl ethanol.

The products of the reaction were determined by EC-IRRAS. The spectra measured with s-polarized light between 0.05 V_{RHE} and 1.1 V_{RHE} showed formation bands at 1174 cm^{-1}, 1199 cm^{-1}, 1259 cm^{-1}, 1295 cm^{-1}, 1359 cm^{-1} and 1435 cm^{-1}. The bands start to appear at 0.3 V_{RHE}. The similar features were observed with p-polarized light. Additional band was detected at 1690 cm^{-1}, which is overlapping with water-band region.

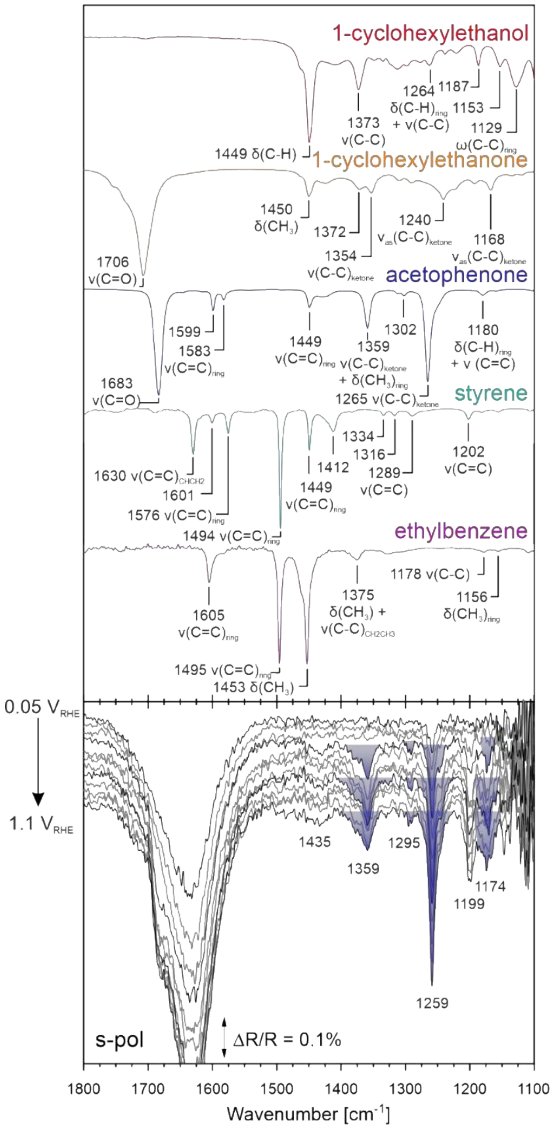

Figure P7.3: ATR IR reference spectra of 1-cyclohexyl ethanol and possible products of its dehydrogenation (top), potential dependent EC-IRRAS measured with s-polarized light (bottom).

We assign bands at 1174 cm^{-1}, 1259 cm^{-1}, 1259 cm^{-1}, 1359 cm^{-1} and 1690 cm^{-1} to the formation of acetophenone. The bands have shoulders at 1259 cm^{-1} and 1359 cm^{-1}, which indicate that a fraction of 1-cyclohexylethanone is also formed. The band at 1450 cm^{-1} is related to vibrations of a C-H bond and cannot be assigned easily to a single molecule. The band at 1199 cm^{-1} is assigned to an unknown decomposition product. The presence of the acetophenone's bands in both, s-polarized and p-polarized, spectra shows that it desorbs from the surface and is present in the solution.

EC-IRRA spectra were measured at 0.4 V_{RHE} consisting of three cycles. In the first cycle, all bands were observed as described above. In the second and third cycle, only the bands at 1199 cm^{-1} and 1259 cm^{-1} remain.

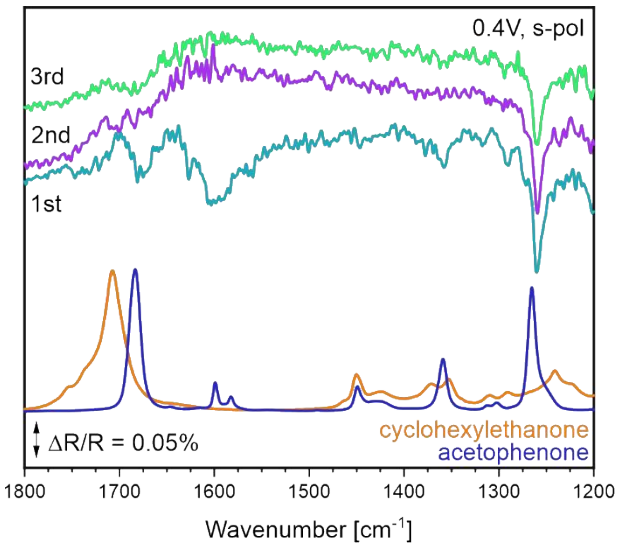

Figure P7.4: Time evolution of EC-IRRAS bands measured with s-polarized light at 0.4 V_{RHE}.

Summary

The thesis was conducted under the bilateral cotutelle agreement between the Charles University in Prague and the Friedrich-Alexander-Universität Erlangen-Nürnberg. It supported a long-lasting cooperation and transfer of knowledge between these institutions. During this thesis, a new EC cell designed at FAU was successfully implemented into the experimental setup at CU. The focus of this thesis lies on the model electrocatalytic studies of metal and metal-oxide based catalysts for application in energy relevant reactions and hydrogen economy. Due to the wide range of experimental methods, it was possible to address different aspects of model electrocatalysis and demonstrate their applicability to various (electro-)catalytic systems – namely Pt single crystal, Co3O4(111), Pt/Co3O4(111), Pd/Co3O4(111), and ceria/Pt. The main findings of the individual studies are summarized as follows:

1) **Properties of Pt/Co3O4(111) in UHV:** Pt forms on Co3O4(111) a highly dispersed structure. The interaction between Pt and Co3O4(111) results in significant charge transfer, which is also predicted by DFT calculations. The analysis of Bader charges shows positive charge on Pt atoms at the metal-oxide interface. The atomically dispersed Pt2+ and Pt4+ may substitute surface Co2+ and sub-surface Co3+ ions, respectively. In the presence of water, Pt4+ can be stabilized at FCC sites and form triaqua complex suppressing the sub-surface substitution.

2) **Properties of Pd/Co3O4(111) in UHV:** Analogically to Pt, Pd species on Co3O4(111) are highly dispersed and undergo a substantial charge transfer with Co3O4(111). The

transferred charge in the substrate is delocalized over top two layers. SRPES identified two main contribution, which correspond to atomically dispersed Pd2+ species, and small Pdδ+ aggregates or Pd4Ox clusters. The depth profiling shows that above mentioned Pd species forms up to 2 ML thick clusters on top of which metallic Pd0 nanoparticles grow.

3) **Stability of Pd/Co3O4(111) under humid and oxidizing conditions:** After exposure to oxygen, Pd nanoparticles oxidize and form PdO layer. The degree of oxidation increases with increasing temperature. PdO is stable in the whole studied temperature range between 300 and 700 K. However, it decomposes after annealing in UHV yielding metallic Pd0 nanoparticles above 500 K. The oxidiation to PdO is accompanied by diffusion of Pd into Co3O4(111) and further Ir(100). Whereas the diffusion into Co3O4(111) is reversible, the diffusion into Ir(100) is irreversible. The exposure to humid environment does not affect Pd oxidation state.

4) **Stability of supported Pd nanoparticles in electrochemical environment:** In contrast with Co3O4 supported Pd, HOPG supported Pd forms metallic Pd0 hemispherical nanoparticles due to weaker electronic metal-support interaction. Immersion of both types of Pd nanoparticles into alkaline electrolyte at potentials between 0.5 VRHE and 1.1 VRHE has no major effect on their oxidation state. At potentials between 1.3 and 1.5 VRHE, the formation of PdO is observed, which is more pronounced on Pd/Co3O4(111) than on Pd/HOPG. PdO is reduced back to Pd0 after returning to initial potential of 0.5 VRHE.

5) **Stability of ceria/Pt in electrochemical environment:** This study demonstrated structural effect on stability of ceria nanoislands in alkaline environment. Large nanoislands with straight edges are stable at potentials between -0.05 VRHE and 0.9 VRHE. On the other hand, small nanoislands with round edges are unstable and undergo transition to amorphous ceria hydrate. Charge analysis in the CVs revealed interesting behavior of H atoms adsorbed on Pt(111). These atoms reversibly diffuse and intercalate at the Pt/ceria interface allowing to accommodate H also on the Pt surface covered by ceria.

6) **Anchoring of porphyrin to Co3O4(111):** It is possible to anchor monophosphatophenyl-triphenyl porphyrin (MPTPP) to Co3O4(111) from a solution. MPTPP binds to the surface via phosphonic acid functionality to Co2+ surface atom in the form of chelating tridentate. The binding motif is stable in the potential range of 0.3 – 1.3 VRHE. The choice of solvent (dichloromethane or ethanol) has no effect on binding motif. However, a co-adsorption of additional species was observed when adsorbing from DCM. The co-adsorbed species are blocking the adsorption sites resulting in lower porphyrin coverage than for adsorption from ethanol.

7) **Electrooxidation of 1-cyclohexylethanol:** Pt(111) shows in comparison with Pt(100) and Pt(110) the highest activity towards the oxidation of 1-cyclohexyl ethanol with the onset potential of 0.3 VRHE . However, all three surfaces quickly deactivate due to poisoning effect of decomposition products. EC-IRRAS identifies two products of 1-cyclohexyl ethanol oxidation – acetophenone and 1-cyclohexyl ethanone. The presence of acetophenone shows that it is possible to use and fully dehydrogenate two hydrogen storage functionalities in one molecule – cyclohexyl ring and secondary alcohol. However, finding a highly selective catalyst preventing the decomposition of the product will be the key factor for a potential use of this molecule as an electrochemically active liquid organic carrier (EC-LOHC).

In general, the presented model studies address different aspects of model electrocatalysis. The main focus was on the properties and stability of metal-oxide catalysts combining the noble metals (Pt, Pd) with reducible oxides (Co_3O_4, CeO_2). The results demostrated a strong impact of EMSI on the structural parameters of the supported metal nanoparticles, their oxidation state and consequently their stability in the electrochemical environment and their electrocatalytic properties. In addition, futher aspects of model electrocatalysis such as the adsorption of molecules from a solution and the identification of products of electrochemical reactions were studied. The presented findings clearly show the importance of model electrocatalysis and its role in the design, development and optimization of novel highly active and selective electrocatalysts.